Flow of an elasto-viscoplastic fluid around a flat plate: Experimental and numerical data

Fiacre Ahonguio, Laurent Jossic, Albert Magnin, Frederic Dufour

Flow of an elasto-viscoplastic fluid around a flat plate: Experimental and numerical data

Fiacre Ahonguio[a], Laurent Jossic [a,*], Albert Magnin[a], Frédéric Dufour[b]

[a] *Univ. Grenoble Alpes, LRP, F-38000 Grenoble, France CNRS, LRP, F-38000 Grenoble, France*
[b] *Univ. Grenoble Alpes, 3SR, F-38000 Grenoble, France CNRS, 3SR, F-38000 Grenoble, France*

This study focuses on the creeping flow of an elasto-viscoplastic fluid around a flat plate moving at a constant velocity. The flow is analyzed both experimentally and numerically. The experiments are performed with a Carbopol gel whose behavior is described by an elasto-viscoplastic model in the numerical analysis. This elasto-viscoplastic model is a 3D Elastic Herschel–Bulkley model implemented in a numerical tool based on the Finite Element Method with Lagrangian Integration Points (FEMLIP). In this model, the yield stress is detected by means of the second invariant of the Cauchy stress tensor and the fluid behaves elastically below the yield stress. The model relies on the understanding of the flow properties especially below the yield stress. After a presentation of the experimental protocol and the numerical method, the numerical and experimental results are compared in terms of kinematic fields and drag coefficients.

1. Introduction

Industrial processes include numerous complex fluids often used for specific needs. Most of these fluids exhibit a solid-fluid transition, i.e. they behave as an elastic solid when they are not sufficiently stressed and flow like a fluid above a yield stress. This specificity has a strong impact on their flows around obstacles. These flows which have received a rising interest in the latest years have been recently reviewed by Balmforth et al. [1] and Coussot [2]. The present study focuses on the simulation of the non-inertial flow of a yield stress fluid around a flat plate with adherence conditions at its wall. This topic which represents a fundamental topic of fluid mechanics has received little consideration in the literature. It has been theoretically considered by Oldroyd [3–4]. Using a Bingham model, he shows for high Oldroyd numbers, i.e. the ratio between plastic and viscous effects, that the fluid is rigid everywhere except in a thin layer where both viscous and plastic effects coexist. The results of Oldroyd have been called into question by the analytical studies of Piau [5] and Piau and Debiane [6]. Piau and Debiane [6] have analyzed the evolutions of the drag coefficient and the boundary layer thickness around a flat plate. By describing the liquid or yielded region with a viscoplastic model and the solid or unyielded region with the Hooke constitutive equation and by using a linear friction law, they predict a lens-shaped boundary layer whose thickness at the mid-plate increases both with the length of the plate and the flow velocity.

The flow of a yield stress fluid around an adhesive flat plate has also been analyzed experimentally [7–11]. Brookes and Whitmore [7] have studied the static drag force of a plate immersed in a Bingham plastic fluid. They observed that this force is directly proportional to the immersed area of the plate. For a wide velocity range, Boujlel et al. [9] have measured the drag force and the velocity fields in the vicinity of a plate during its displacement. They observed that the boundary layer thickness does not vary a lot with the velocity; a puzzling result contradicting the theoretical analysis of Piau and Debiane [6] which predicts a decrease of this thickness towards zero for zero velocity. In addition, Ahonguio et al. [11] have recently investigated the creeping flow of a yield stress fluid around a flat plate. They have particularly analyzed the influences of both the slip and the velocity on the drag force and the kinematic fields. Their results corroborate the weak influence of the velocity on the yielded and unyielded regions of the flows. They also reveal that slip has a significant influence both on these regions and the drag coefficient.

The only numerical results concerning the non-inertial flow of elasto-viscoplastic materials over an adhesive blade have been obtained by Ferreira et al. [12]. Their analysis was performed with the thixotropic elasto-viscoplastic model proposed by de Souza Mendes [13] in which the Stokes equations are solved by a numerical code with finite elements based on the Galerkin least squares method. Ferreira et al. have only analyzed kinematics without addressing drag force calculations. They observed that elasticity

* Corresponding author. Fax: +33 4 56 52 01 97.
E-mail address: Laurent.jossic@grenoble-inp.fr (L. Jossic).

Nomenclature

a: half-height of the plate (m)
A: Lateral section (m^2)
D: strain rates tensor
D_{II}: second invariant of the strain rates tensor (s^{-1})
D_v: viscous strain rates tensor
D_{vII}: second invariant of the viscous strain rates tensor (s^{-1})
D_e: elastic strain rates tensor
D_{eII}: second invariant of the elastic strain rates tensor (s^{-1})
F_d: drag force (N)
f_{ext}: external forces (N)
G: shear elasticity modulus (Pa)
G': elastic modulus (Pa)
G": viscous modulus (Pa)
K: consistency (Pa s^n)
m: coefficient (-)
n: shear-thinning index (-)
p: pressure field
Ra: roughness (m)
U: norm of the velocity ($m.s^{-1}$)
U_0: tank velocity ($m.s^{-1}$)
U_r: transverse velocity ($m.s^{-1}$)
U_z: axial velocity ($m.s^{-1}$)
v: velocity field
r: transverse unitary vector (m)
Δt_e: elastic time step (s)
T: temperature (°C)
W: vorticity or rate-of-rotation tensor
z: axial unitary vector (m)

Greek symbols
β: coefficient ()
Γ: elasticity number ()
ε: strain tensor
ε_{II}: second invariant of the strain tensor ()
$\boldsymbol{\varepsilon}^*_{II}$: non dimensional second invariant of the strain tensor corresponding to $\frac{\varepsilon_{II}}{(\frac{\tau_0}{G})}$ ()
$\dot{\gamma}$: shear rate (s^{-1})
η_{eff}: effective viscosity (Pa.s)
η': apparent viscosity (Pa.s)
ρ: density ($kg.m^{-3}$)
τ: shear stress (Pa)
$\boldsymbol{\tau}$: deviatoric stress tensor
τ_{II}: second invariant of the deviatoric stress tensor (Pa)
$\boldsymbol{\tau}^*_{II}$: non dimensional second invariant of the deviatoric stress tensor corresponding to $\frac{\tau_{II}}{\tau_0}$ ()
τ_0: yield stress (Pa)
τ_w: wall shear stress (Pa)
τ^*_w: non-dimensional wall shear stress corresponding to $\frac{\tau_w}{\tau_0}$ ()

Non-dimensional numbers
C^*_d: drag coefficient
$C^*_{d,\infty}$: asymptotic drag coefficient
Od: Oldroyd number
r^*: non-dimensional transverse unitary vector corresponding to r/a
Re: Reynolds number
U^*_z: non-dimensional velocity corresponding to U_z/U_0
z^*: non-dimensional axial unitary vector corresponding to z/a

changes the shape of the yielded and unyielded regions close to the blade. They also observed a decrease in the extent of the unyielded regions following an increase of the velocity.

The scarcity of numerical data is due to the difficulty of modeling elasto-viscoplastic behavior. Such behavior includes a solid-fluid transition often described by the Von-Mises criterion. This transition leads to a discontinuity which is not straightforward to describe numerically. In order to alleviate this discontinuity, most numerical analyses are performed with viscoplastic models in which the solid-fluid transition is regularized. The most common regularized models are the two-viscosity model and the Papanastasiou model [14–15] which substitute the behavior below the yield stress by a highly viscous behavior. Even though the regularization alleviates the simulations, it does not correctly describe the solid-fluid transition of elasto-viscoplastic materials. What is more, it does not enable to analyze the influence of the elasticity on flow properties. In order to better describe elasto-viscoplastic materials, advanced models have been proposed by Saramito [16] and Dimitriou et al. [17]. The latter authors have proposed an Elastic Herschel-Bulkley (EHB) model for describing Carbopol gels behavior. Their model relies on a strain decomposition in a plastic and an elastic contributions. The elastic contribution is taken into account below and above the yield stress. The model used in this study is similar to the EHB model; it will be described later.

The present study aims to compare the numerical and experimental data concerning the creeping flow of a Carbopol gel around an adhesive plate. The numerical data have been obtained by simulations performed with a code based on the Finite Element Method with Lagrangian Integration Points (FEMLIP). The gel behavior is described with an elasto-viscoplastic model. Firstly, the experimental framework is presented. Then, the numerical method and the model used for the simulations are described. Finally, the experimental and numerical results are compared.

2. Experimental framework

2.1. Rheological characterization

The experiments were performed with an aqueous gel of polymer, namely Carbopol 940 [18]. The studies [1–2,17,19] provide a critical and complete view of the data concerning this yield stress fluid which is a concentrated suspension of deformable micro-gels swollen with a solvent. The yield stress of Carbopol gel stems from the spatial packing of the micro-gels whose size ranges from 2 to 20 µm [19]. Carbopol gel 940 is characterized by its viscoplastic and non-thixotropic behavior [17,19–23], its good stability over time and its transparency. The gel used is concentrated at 1 wt.% of Carbopol 940. Its pH is approximately 7.3 and its density about 1000 $kg.m^{-3}$. The rheological behavior of the gel has been finely characterized by simple shear measurements performed with an ARES rheometer manufactured by TA Instruments. The measurements were completed with a cone-plate cell at controlled speed, controlled temperature and controlled evaporation rate, for shear rates between 10^{-4} and 30 s^{-1}. The surfaces of the cone-plate cell were covered with sandpaper with a roughness of approximately 200 µm in order to avoid any slip. The cone used has an angle of 0.04 rad and a diameter of 49 mm.

The rheological behavior of the gel can be modeled by the Herschel–Bulkley model completed by the Hooke's model.

$$\begin{cases} \tau_{ij} = 2\left(\dfrac{\tau_0}{\sqrt{-4D_{II}}} + K\sqrt{-4D_{II}}^{n-1}\right)D_{ij} & \text{if } -\tau_{II} > {\tau_0}^2 \\ \tau_{ij} = 2G\varepsilon_{ij} & \text{if } -\tau_{II} \leq {\tau_0}^2 \end{cases} \quad (1)$$

where τ_0, K and n represent the yield stress, the consistency and the shear thinning index respectively. G is the shear elasticity

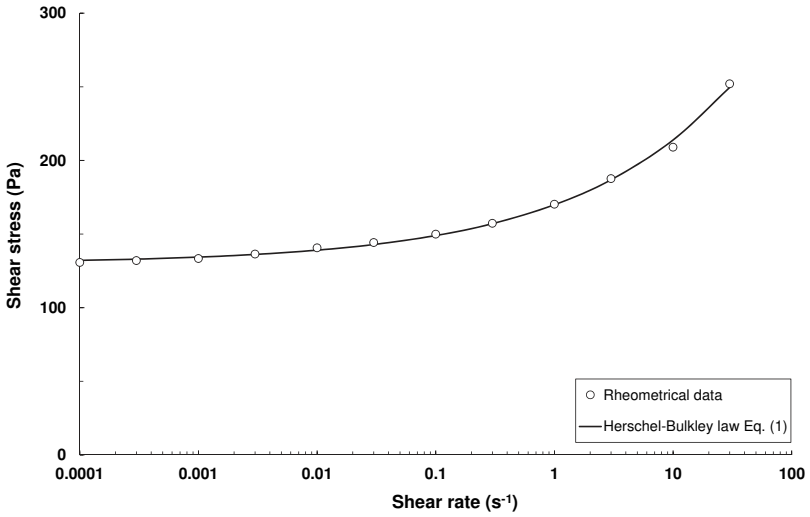

Fig. 1. Flow curve of the gel.

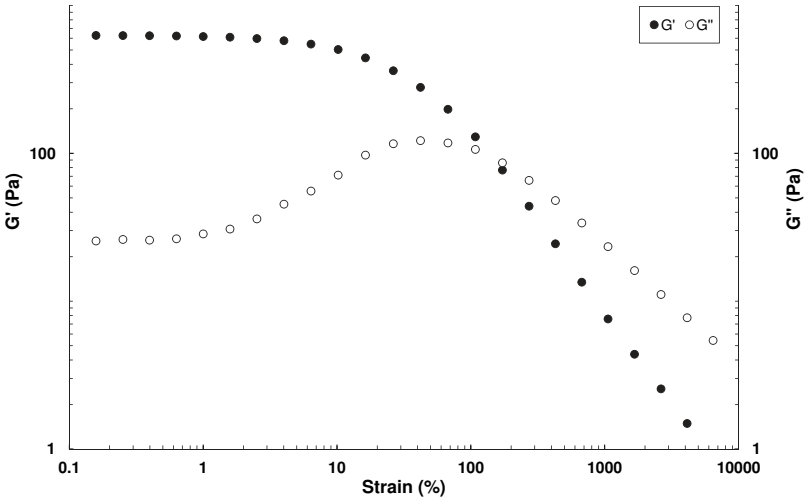

Fig. 2. Evolution of the elastic and viscous moduli as a function of the strain.

Table 1
Rheometrical properties of the gel.

τ_0 (Pa)	K (Pa.s^n)	n	G (Pa)
131	39	0.32	620

modulus, ε is the strain tensor, $D_{II} = -\frac{1}{2}tr(D_{ij}^2)$ and $\tau_{II} = -\frac{1}{2}tr(\tau_{ij}^2)$ are the second invariants of the strain rates and deviatoric stress tensors respectively. It is worth noting that since the Hooke's model is only limited to small strains, the neoHookean model [24–25] is more likely to better describe the gel behavior below the yield stress.

Fig. 1 represents the evolution of the shear stress as a function of the shear rate under steady conditions at T = 23°C for the Carbopol gel. The measurement uncertainties can be estimated at about 10%. The parameters of the Herschel-Bulkley model are recapped in Table 1. The evolutions of the elastic and viscous moduli G' and G'' as a function of the strain are provided in Fig. 2. They were obtained by dynamic frequency tests performed at a frequency of 1 Hz and T = 23°C. The plateaus of G' and G'' are about 625 Pa and 30 Pa respectively. The linear domain ends at a strain of about 1% and the cross-over point between G' and G'' is at a strain of about 144% (G' = G'' = 92 Pa).

2.2. Experimental set-up

Since the experimental device has already been presented in [11], it is only briefly described here. The plate is a square with 50 mm per side, 0.9 mm of thickness and a roughness Ra = 200 µm. It is immersed in a square base parallelepiped tank containing Carbopol gel. This tank is moved at constant controlled velocities ranging from 1 to 250 µm s^{-1}. With regards to the tank dimensions 200 × 200 × 300 mm and the involved velocities, wall effects can be neglected.

The drag force on the plate has been measured with a weighing balance with a precision of 0.1 g. It corresponds to the force measured in steady state after the buoyancy force has been subtracted. The measurement uncertainties for the drag coefficient can be estimated at 15%. They stem from undesirable effects such as friction on the nylon threads and the rigid plane parallel rod used for linking the plate to the weighing balance.

The drag coefficient is defined by Eq. (2) in which F_d, A, $C^*_{d,\infty}$ and Od are respectively the drag force, the lateral surface of the

plate, the asymptotic drag coefficient and the Oldroyd number defined in Eq. (14), and β and m are coefficients.

$$C_d^* = \frac{F_d}{\tau_0 * A} = C_{d,\infty}^* + \frac{\beta}{Od^m} \tag{2}$$

The velocity fields have been visualized by the PIV technique. To this end, the gel was seeded with silver-coated hollow glass particles whose diameter varies between 5 and 30 µm and whose density is approximately 1400 kg m^{-3}. The flow was illuminated by a continuous laser, with a wavelength of 532 nm and a power of 100 mW. The mesh used in the PIV software Flow Manager V4.71 corresponds to 46×34 vectors and to interrogation areas of 32 pixels per side. The measurement uncertainties can be estimated at 10% for the kinematic fields.

3. Numerical method

3.1. Description of the FEMLIP

The Finite Element Method with Lagrangian Integration Points (FEMLIP) has been proposed by Moresi and Solomatov [26] and Moresi et al. [27]. It originates from the Particle-In-Cell method for which the numerical integration weight is recomputed in each configuration in order to keep the finite element properties of the Gaussian integration scheme. It is a hybrid method coupling the Eulerian and Lagrangian approaches. The former approach is used for the mesh points which are spatially fixed nodes while the latter is used for the integration points which are a set of material points moving in a fixed mesh towards a new configuration. The fixed mesh enables to avoid the spurious distortion of the mesh and the Lagrangian property of particle advection avoids the numerical diffusion problems which can especially appear in the modeling of material interactions. The material points carrying the constitutive and history variables, are used in a given configuration as integration points in order to compute the nodal velocity field. They are formally separated from the calculation points. In order to couple them, a quadrature of non-standard elements in which the particles in each element serve as integration points can be used. At the end of each calculation step, the new location of particles is updated based on the velocity field by means of Finite Elements shape functions.

FEMLIP has already been used in geotechnics for analyzing concrete flows and landslides [28–32]. It can be used for studying numerous phenomena such as large strain phenomena and free surface flows. It can also be used for predicting the extent of sheared zones and the rheometrical parameters of a material. In the present study, an elasto-viscoplastic model has been implemented in a numerical tool based on the FEMLIP [33]. This model is a 3D elastic Herschel-Bulkley model in which the material behavior is elastic below the yield stress and viscoplastic above it. Hence, the flow properties can be analyzed below and above the yield stress.

3.2. Mechanical modeling

The mechanical behavior of the gel can be described by Eqs. (3), (4) and (5). The deviatoric stress tensor $\boldsymbol{\tau}$ follows the Maxwell model, Eq. (3). In this equation, the strain rate tensor $\mathbf{D}$ is splitted into a viscous and an elastic contribution, $\mathbf{D_v}$ and $\mathbf{D_e}$, respectively. Above the yield stress, the shear stress component is twice the product of the viscous strain rate tensor $\mathbf{D_v}$ by an apparent viscosity η', Eq. (4). This apparent viscosity depends on the shear thinning index n, the consistency K, the yield stress τ_0 and the second invariant of the viscous strain rates tensor D_{vII}.

$$\begin{cases} \dfrac{\dot{\tau}_{ij}}{2G} + \dfrac{\tau_{ij}}{2\eta'} = D_{ij} = D_{vij} + D_{eij} \\ \tau_{ij} = \left[\dfrac{\tau_0}{2D_{vII}} + K(2D_{vII})^{n-1} \right] D_{vij} = 2\eta' D_{vij} \quad \text{if} - \tau_{II} > \tau_0^2 \\ D_{vII} = \left[\dfrac{1}{2} \left(D_{11}^2 + D_{22}^2 + 2^* D_{12}^2 \right) \right]^{\frac{1}{2}} \end{cases} \tag{3, 4, 5}$$

The Stokes' equations solved in the simulations are given by Eqs. (6) and (7) in which f_{ext}, p and v represent the external forces, the pressure and the velocity field respectively. X_i and $X_{,i}$ correspond to the component and the spatial derivative along the direction i of the field X.

$$\begin{cases} (f_{ext})_i + \tau_{ij,j} - p_{,i} = 0 \\ v_{i,i} = 0 \end{cases} \tag{6, 7}$$

Eq. (8) provides the temporal discretization of the convective derivative $\dot{\tau}_{ij}$ with the elastic time step Δte chosen to capture the elastic stress variations. This time step can be different from the advection time step chosen for updating particles locations. $\mathbf{W}$ represents the vorticity tensor which corresponds to the antisymmetric part of the velocity gradient.

$$\dot{\tau}_{ij}^{t+\Delta te} = \frac{\tau_{ij}^{t+\Delta te} - \tau_{ij}^{t}}{\Delta te} + \tau_{ij}^{t*} W_{ij}^{t} - W_{ij}^{t} * \tau_{ij}^{t} \tag{8}$$

Coupling Eqs. (3) and (8) leads to the discretized elastic Herschel-Bulkley model used in the simulation.

$$\begin{cases} \tau_{ij}^{t+\Delta te} = \eta_{eff} \left[2^* D_{ij}^{t+\Delta te} + \dfrac{\tau_{ij}^{t}}{G\Delta te} + \dfrac{\tau_{ij}^{t*} W_{ij}^{t} - W_{ij}^{t} * \tau_{ij}^{t}}{G} \right] \\ \eta_{eff} = \eta' \dfrac{G^* \Delta te}{G^* \Delta te + \eta'} \end{cases} \tag{9, 10}$$

η_{eff} represents the effective viscosity of the gel. Eqs. (6) and (9) lead to Eqs. (11) and (12).

$$\begin{cases} (f_{ext})_i + 2\eta_{eff}\, D_{ij}^{t+\Delta te} + (f_e)_i - p_{,i} = 0 \\ (f_e)_i = \eta_{eff} \left[\dfrac{\tau_{ij}^{t}}{G\Delta te} + \dfrac{\tau_{ij,j}^{t} * W_{ij,j}^{t} - W_{ij,j}^{t} * \tau_{ij,j}^{t}}{G} \right] \end{cases} \tag{11, 12}$$

Eqs. (11) and (12) are solved iteratively at each time step until a stability criterion is reached based on the residual of Eq. (11). It is worth noting that the modeling used for describing the elasto-viscoplastic behavior of the gel does not require any regularization in order to alleviate the discontinuity due to the solid-fluid transition. Moreover, it takes into account the elastic effects both below and above the yield stress. This modeling is similar to the one proposed by de Souza Mendes and Thompson [34], which is an improved version of the modeling provided in [13], in the limit of no thixotropy and zero retardation viscosity.

3.3. Problem statement

Fig. 3 represents the flow configuration considered in this simulation. Only one half of the simulation domain has been considered for symmetry reasons. The complete domain is bi-dimensional with a length $L = 0.3$ m and a width $H = 0.2$ m. The plate is adhesive and has no thickness. It is fixed and located at $r = 0$, between $z = 0.1$ m and $z = 0.2$ m. The boundary conditions are such that both the upstream and downstream velocity profiles are uniform with a constant velocity U_0. The fluid is assumed to adhere to the wall of the plate; hence the velocity is set equal to zero at this

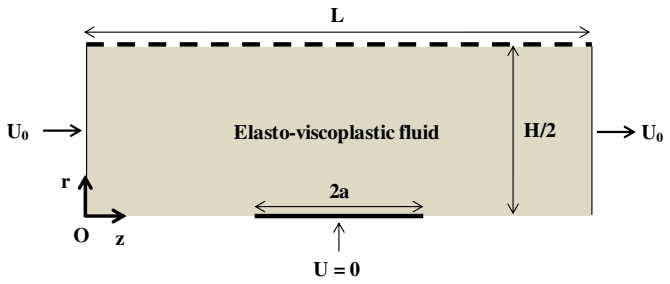

Fig. 3. Problem statement.

wall. Apart from the boundary conditions, the initial conditions for the overall field are set to zero.

Three regular meshes were used: $M1 = 97 \times 33$, $M2 = 48 \times 57$ and $M3 = 72 \times 80$ elements respectively along the z-axis and the r-axis. The simulations were performed with an elastic time step Δte about 0.1 s and a convergence criterion on the residual of 10^{-5}. The rheological parameters used in the simulations are the ones of the gel considered in the experiments: $\tau_0 = 131$ Pa, $K = 39$ Pa.s^n, $n = 0.32$ and $G = 620$ Pa. The half-length of the plate a and the velocity U_0 are used as length and velocity scales respectively.

Based on Eq. (1) and the mechanical behavior laws, the Reynolds, Oldroyd [3,4] and elasticity numbers can be expressed as follows:

$$\mathrm{Re} = \frac{\rho U_0^{2-n} a^n}{K}, \quad \mathrm{Od} = \frac{\tau_0}{K\left(\frac{U_0}{a}\right)^n} \quad \text{and} \quad \Gamma = \frac{G}{K\left(\frac{U_0}{a}\right)^n} \quad (13, 14, 15)$$

where ρ represents the fluid density. The ratio between Od and Γ represents a critical deformation. For a given material, this ratio is constant and corresponds to the deformation which enables the solid-fluid transition. The simulations were performed for Reynolds numbers ranging from 4.10^{-8} to 0.11, Oldroyd numbers ranging from 3 to 49 and for elasticity numbers ranging from 14 to 510.

4. Results and discussions

4.1. Kinematic fields

This section compares the experimental and numerical velocity fields in the vicinity of the plate. It focuses on the velocity profiles at the mid-plate and at the leading and trailing edges. Then, it presents the velocity fields and the fields of the second invariants of the strain rate, the strain and the deviatoric stress tensors.

4.1.1. Velocity profiles

Fig. 4 provides the experimental and numerical dimensionless axial velocity profiles at the mid-plate as a function of $r^* = r/a$. The numerical profiles obtained with the three meshes, are all obtained by averaging 10 velocity profiles regularly spaced by 10 increments for reducing numerical fluctuations. They give similar results even if meshes M2 and M3, more refined in the r direction, provide more precise results in the vicinity of the plate. Considering the experimental uncertainties, the numerical profiles are overall in good agreement with the experimental profile. The wall velocity gradient computed with the meshes M2 and M3, is around $0.04\,s^{-1}$ and estimated at $0.06\,s^{-1}$ for the experimental data.

The good agreement between the experimental and numerical results can also be observed in Fig. 5 which represents the dimensionless axial velocity profiles at the leading and trailing edges of the plate. The numerical profiles are averaged as previously explained. However, some fluctuations can be observed in the vicinity of the trailing edge depending on the mesh. These fluctuations, due to high velocity gradients at the trailing edge, are not observable on the profile obtained with the mesh M3. As already observed experimentally in flows around obstacles [35–37], the experimental velocity profiles are not symmetrical because of the fluid elasticity [38]. This asymmetry is correctly reproduced numerically by the elasto-viscoplastic model; differences with the experimental data are lower than a few percent. It has not been observed by Piau and Debiane [6] who predict a symmetrical lens-shaped boundary layer around the plate.

Furthermore, the numerical and experimental thicknesses of the boundary layer are overall the same. Defining this thickness with the criterion $U_z = 0.99U_0$, it is about 9.5 mm numerically and 10 mm experimentally. These values which confirm the ones obtained by Boujlel et al. [9] are twice higher than the theoretical values predicted by Piau and Debiane [6] at $Od = 21$. The difference can be explained by the viscoplastic model used to describe the gel behavior in their analysis. Such a model does not completely describe the gel behavior since it does not take into account the elastic properties of the material.

4.1.2. Fields of the second invariant of the strain rate tensor

Fig. 6 represents the numerical fields of the second invariant D_{II} of the strain rate tensor for two materials: the one used in the experiments (a) and a more rigid material (b) whose elastic modulus

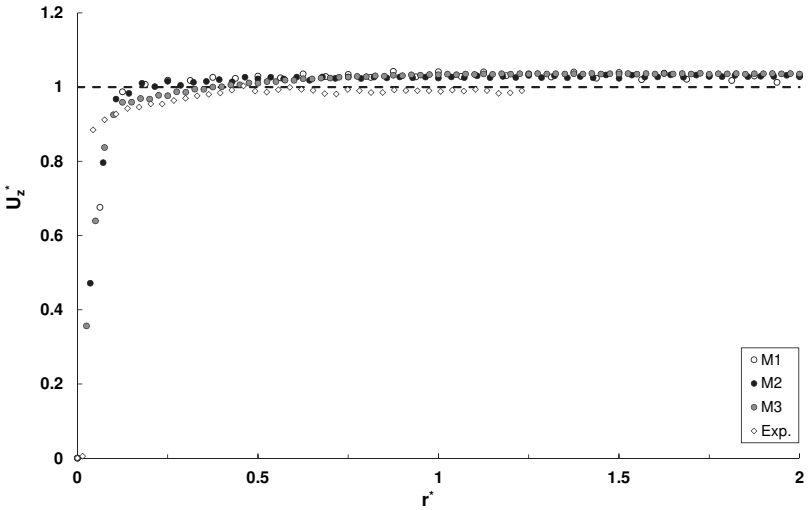

Fig. 4. Non-dimensional axial velocity profiles as a function of r^* at the mid-plate. Numerical: $Od = 21$, $\Gamma = 102$. Experimental: $Od = 16$, $\Gamma = 102$.

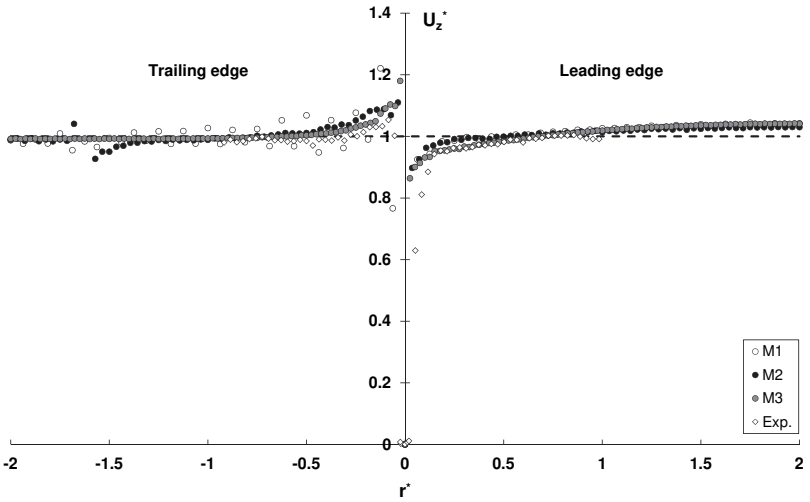

Fig. 5. Non-dimensional axial velocity profiles as a function of r^* at the trailing and leading edges. Numerical: Od = 21, Γ = 102 Experimental: Od = 16, Γ = 102.

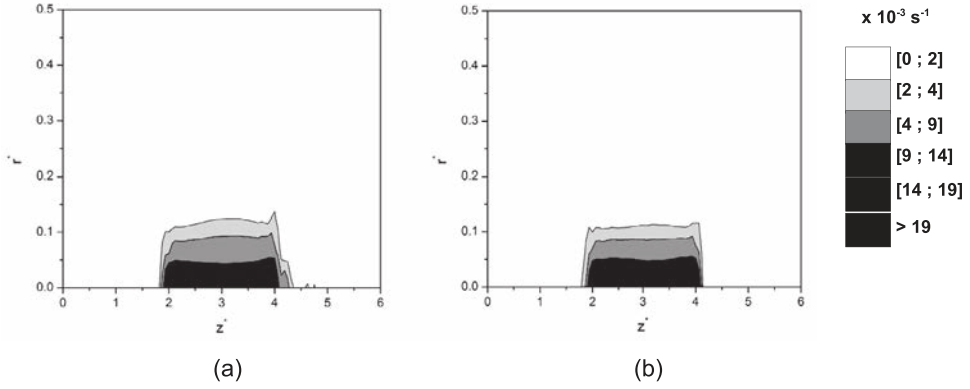

Fig. 6. Numerical fields of the second invariant of the strain rates tensor: (a): Γ = 102 and (b): Γ = 510. Od = 21.

G is five times higher; all other rheological parameters being equal. Considering the material used in the experiments, the field shows two main flow regions: a sheared zone close to the plate and a rigid mobile zone far from the plate. The sheared zone corresponds to colored zones in which D_{II} decreases progressively from highest values at the wall to values lower than 0.002 s^{-1} in the rigid mobile zone. Choosing $D_{II} \leq 0.002\ s^{-1}$ as a criterion for delineating the boundary between the sheared and rigid mobile zones, the thickness of the liquid region is about 6 mm.

Figs. 6a and b illustrate the influence of elasticity on the flow morphology. In the case of the rigid material, the two flow regions previously evoked are also observed. However, the values of D_{II} along the plate are higher than 0.019 s^{-1}, i.e. the material is less deformable than the one used in the experiments for which the values obtained at the wall are about 0.014 s^{-1}. The liquid region seems to be symmetrical between the leading and trailing edges of the plate. Its thickness is about 5 mm; approximately 15% lower than the thickness found with the material used in the experiments. The symmetry observed for the rigid material corroborates the symmetrical lens-shaped observed by Piau and Debiane [6]. Hence, the asymmetry is due to the elastic properties of the material.

4.1.3. Fields of the second invariants of the strain and deviatoric stress tensors

Fig. 7 represents the numerical fields of the non-dimensional second invariants of the strain $\varepsilon_{II}^* = \frac{\varepsilon_{II}}{(\frac{\tau_0}{G})}$ (Figs. 7a and b) and the deviatoric stress $\tau_{II}^* = \frac{\tau_{II}}{\tau_0}$ tensors (Figs. 7c and d) for the two materials previously considered. The ratio $\frac{\tau_0}{G}$ represents the critical deformation enabling the solid-fluid transition of the material. Hence, sheared zones correspond to $\varepsilon_{II}^* \geq 1$. The fields of ε_{II}^* show that the deformation spreads in all the material. In the case of the more rigid material, the deformations are higher in the all the flow field. They start with higher values in the immediate vicinity of the plate and progressively decrease to 0 far from it. Overall, the highest values of the deformations are computed along the plate and at its leading and trailing edges. In the case of the more rigid material, the extent of the sheared zone is approximately 3 times wider. The computed fields of τ_{II}^* are similar. They start with values higher than 1, corresponding to the boundary between the sheared and non-sheared zones, in the immediate vicinity of the plate. Then, they decrease progressively towards 0.25 far from the plate where the material is less affected by the presence of the plate.

4.2. Wall shear stress and drag coefficient

This section focuses on the drag force undergone by the plate. It provides the evolution along the plate of the wall shear stress numerically computed. Then, it compares the numerical and experimental evolutions of the drag coefficient as a function of the Oldroyd number.

4.2.1. Wall shear stress

Fig. 8 represents the numerical evolutions of the dimensionless wall shear stress $\tau_w^* = \frac{\tau_w}{\tau_0}$ along the plate at Od = 21 for both

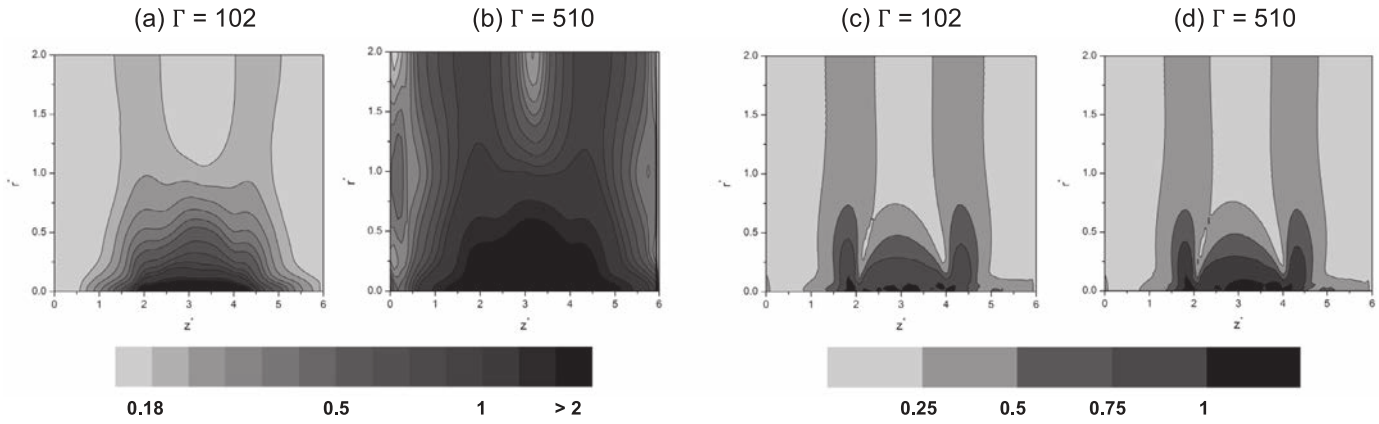

Fig. 7. Numerical fields of the second invariants of the strain tensor (a,b) and the deviatoric stress tensor (c,d). Od = 21.

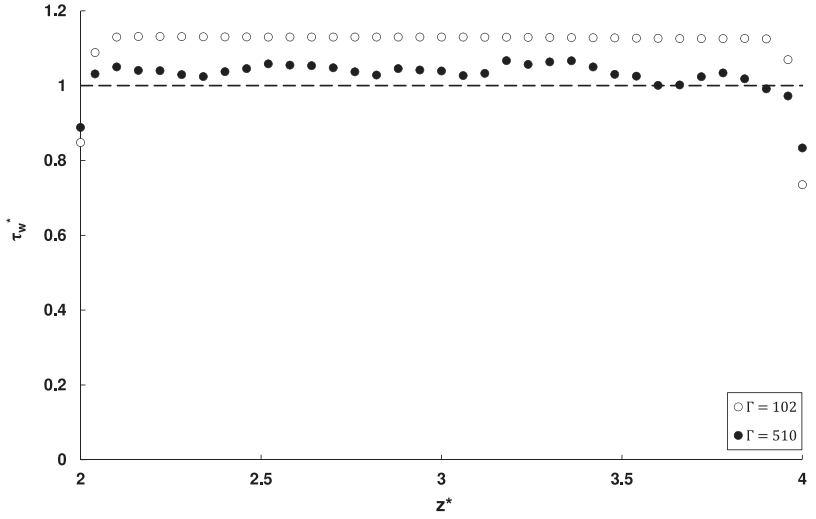

Fig. 8. Evolutions of the non-dimensional wall shear stress along the plate for two materials. Od = 21.

materials considered in Fig. 6. Considering the material used in the experiments, i.e. $\Gamma = 102$, the dimensionless wall shear stress is overall constant along the plate. Its value is about 1.13 except at the leading and trailing edges where the values are about 0.85 and 0.74 respectively. This difference between the leading and trailing edges corroborates the asymmetry observed in the velocity profiles. Indeed, due to the elasticity of the gel, the leading edge of the plate is a region where the gel is compressed. This results in an increase of the wall stress. However, the trailing edge is a region characterized by a relaxation of the gel. There, the wall shear stress is lower than the one at the leading edge.

Fig. 8 also provides the evolution of the wall shear stress along the plate for the more rigid material with $\Gamma = 510$. The evolution is overall similar to the one of the material with $\Gamma = 102$ although it is quite symmetrical like the field of D_{II}, Fig. 6. However, since the material is more rigid, the wall shear stresses are lower for $\Gamma = 510$ than for $\Gamma = 102$ except at the leading and trailing edges where they are about 0.88 and 0.83 respectively. The resulting drag coefficient for $\Gamma = 510$ is around 1.02. Hence, the wall shear stress for the rigid material is equal to the yield stress of the material.

4.2.2. Drag coefficient

This section focuses on the evolution of the drag coefficient as a function of the Oldroyd number. Since a change in the Oldroyd number leads to a change in the elasticity number, the computations were performed at a constant critical deformation about 21%. From the wall shear stress along the plate numerically computed, the drag coefficient can be calculated using Eq. (2) and then compared to the experimental value. To this end, the drag force is calculated by the integration of the wall shear stress along the plate.

Table 2
Values of the parameters of Eq. (2).

Analysis	Exp.	Piau and Debiane [6]
$C^*_{d,\infty}$	0.85	1
β	1.64	1.26
m	0.6	0.75

Fig. 9 represents the numerical and experimental evolutions of the drag coefficient as a function of the Oldroyd number. The parameters of Eq. (2) are provided for the experimental evolution in Table 2. Overall, the numerical and experimental data are in good agreement. The theoretical evolution obtained by Piau and Debiane [6] is also represented in Fig. 9. This evolution is similar to the others albeit some differences concerning the values especially for the asymptotical drag coefficient. These differences could stem from the models used to describe the fluid behavior: a viscoplastic

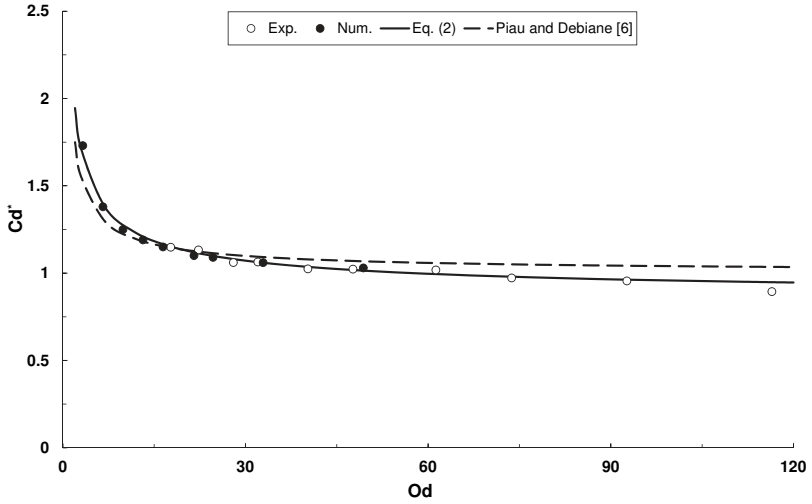

Fig. 9. Evolutions of the drag coefficient as a function of the Oldroyd for a constant critical deformation of 21%.

model for the theoretical analysis and an elasto-viscoplastic model for the numerical analysis. They could also be due to the experimental measurement uncertainties.

5. Conclusion

This study has analyzed the creeping flow of an elasto-viscoplastic fluid around an adhesive plate. It has compared experimental and numerical data. The numerical simulations have been performed using an elasto-viscoplastic model implemented in a numerical tool based on the FEMLIP. The comparison between the experimental and numerical data has highlighted a good agreement both on the kinematic fields and the drag coefficient. The flow asymmetry between the leading and trailing edges of the plate observed experimentally has been reproduced numerically, thus confirming the influence of elasticity. The study has shown the reduction of the extent of the liquid region and a symmetrical profile for more rigid materials. With regards to the good agreements between the experimental and numerical data, the EHB model implemented is a bright tool for analyzing elasto-viscoplastic flows around obstacles.

Acknowledgments

The Laboratoire Rhéologie et Procédés and the Laboratoire 3SR are part of the LabEx Tec 21 (Investissements d'Avenir - Grant agreement n° ANR-11-LABX-0030) and of the PolyNat Carnot Institute (Investissements d'Avenir - Grant agreement n° ANR-11-CARN-030-01).

References

[1] N.J. Balmforth, I.A. Frigaard, G. Ovarlez, Yielding to stress: recent developments in viscoplastic fluid mechanics, Annu. Rev. Fluid Mech. 46 (2014) 121–146.
[2] P. Coussot, Yield stress fluid flows: a review of experimental data, J. Non-Newtonian Fluid Mech. 211 (2014) 31–49.
[3] J.G. Oldroyd, A rational formulation of the equations of plastic flow for a Bingham fluid, Proc. Camb. Philos. Soc 43 (1947) 100–105.
[4] J.G. Oldroyd, Two-dimensional plastic flow for a Bingham fluid. A boundary-layer theory for slow motion, Proc. Camb. Philos. Soc. 43 (1947) 383–395.
[5] J.-M. Piau, Viscoplastic boundary layer, J. Non-Newtonian Fluid Mech. 102 (2) (2002) 193–218.
[6] J.-M. Piau, K. Debiane, The adhesive or slippery flat plate viscoplastic boundary layer for a shear-thinning power-law viscosity, J. Non-Newtonian Fluid Mech. 117 (2004) 97–107.
[7] G.F. Brookes, R.L. Whitmore, The Static Drag on Bodies in Bingham Plastics, Rheol. Acta 7 (2) (1968) 188–193.
[8] J. Boujlel, P. Coussot, Measuring yield stress: a new, practical, and precise technique derived from detailed penetrometry analysis, Rheol. Acta 51 (10) (2012) 867–882.
[9] J. Boujlel, M. Maillard, A. Lindner, G. Ovarlez, X. Chateau, P. Coussot, Boundary layer in pastes – Displacement of a long object through a yield stress fluid, J. Rheol. 56 (2012) 1083–1108.
[10] T. Chevalier, S. Rodts, X. Chateau, J. Boujlel, M. Maillard, P. Coussot, Boundary layer (shear band) in frustrated viscoplastic flows, Europhys. Lett. 102 (48002) (2013) 1–5.
[11] F. Ahonguio, L. Jossic, A. Magnin, Influence of slip on the flow of a yield stress fluid around a flat plate, AIChE J 62 (4) (2016) 1356–1363.
[12] M.R.S. Ferreira, G.M. Furtado, L. Hermany, S. Frey, M.F. Naccache, P.R. de Souza Mendes, External flows of elasto-viscoplastic materials over a blade, in: Proc. of the ENCIT 2014, 15th Brazilian Congress of Thermal Sciences and Engineering, Belém , PA, Brazil, 2014 November 10-13.
[13] P.R. de Souza Mendes, Thixotropic elasto-viscoplastic model for structured fluids, Soft Matt. 7 (6) (2011) 2471–2483.
[14] T.C. Papanastasiou, Flow of materials with yield, J. Rheol. 31 (1987) 385–404.
[15] J. Blackery, E. Mitsoulis, Creeping motion of a sphere in tubes filled with a Bingham plastic material, J. Non-Newtonian Fluid Mech. 70 (1997) 59–77.
[16] P. Saramito, A new constitutive equation for elastoviscoplastic fluid flows, J. Non-Newtonian Fluid Mech. 145 (1) (2007) 1–14.
[17] C.J. Dimitriou, R.H. Ewoldt, G.H. McKinley, Describing and prescribing the constitutive response of yield stress fluids using large amplitude oscillatory shear stress (LAOStress), J. Rheol. 57 (1) (2013) 27–70.
[18] BF Goodrich Literature. Cleveland. 1997.
[19] J.-M. Piau, Carbopol gels: elastoviscoplastic and slippery glasses made of individual swollen sponges, J. Non-Newtonian Fluid Mech. 144 (2007) 1–29.
[20] F. Ahonguio, L. Jossic, A. Magnin, Influence of surface properties on the flow of a yield stress fluid around spheres, J. Non-Newtonian Fluid Mech. 206 (2014) 57–70.
[21] P.C.F. Møller, A. Fall, D. Bonn, Origin of apparent viscosity in yield stress fluids below yielding, Europhys. Lett. 87 (38004) (2009) 1–5.
[22] P.C.F. Møller, A. Fall, V. Chikkadi, D. Derks, D. Bonn, An attempt to categorize yield stress fluid behavior, Philos. Trans. Roy. Soc. A 367 (2009) 5139–5155.
[23] G. Ovarlez, S. Cohen-Addad, K. Krishan, J. Goyon, P. Coussot, On the existence of a simple yield stress fluid behavior, J. Non-Newtonian Fluid Mech. 193 (2013) 68–79.
[24] R. Höhler, S. Cohen-Addad, V. Labiausse, Constitutive equation to describe the nonlinear elastic response of aqueous foams and concentrated emulsions, J. Rheol. 48 (2004) 679–690.
[25] V. Labiausse, R. Höhler, S. Cohen-Addad, Shear induced normal stress differences in aqueous foams, J. Rheol. 51 (2007) 479–492.
[26] L.N. Moresi, V.S. Solomatov, Numerical investigation of 2D convection with extremely large viscosity variations, Physics of Fluids 7 (9) (1995) 2154–2162.
[27] L. Moresi, F. Dufour, H. Muhlhaus, A Lagrangian integration point finite element method for large deformation modeling of viscoelastic geomaterials, J. of Comp. Phys. 184 (2) (2003) 476–497.
[28] H. Muhlhaus, F. Dufour, L. Moresi, B. Hobbs, A director theory for viscoelastic folding instabilities in multilayered rock, Int. J. Solids Struct. 39 (13-14) (2002) 3675–3691.
[29] F. Dufour, G. Pijaudier-Cabot, Numerical modeling of concrete flow. Homogeneous approach, Int. J. Num. Anal. Meth. Geomech. 29 (4) (2005) 395–416.
[30] N. Prime, F. Dufour, F. Darve, Solid-fluid transition modelling in geomaterials, Int. J. Num. Anal. Meth. Geomech. 38 (13) (2014) 1341–1361.
[31] N. Prime, F. Dufour, F. Darve, Unified model for geomaterial solid/fluid states and the transition in between, J. Eng. Mech. 140 (6) (2014) 04014031.

[32] Z. Li, F. Dufour, F. Darve, Hydro-elasto-plastic modelling with a solid/fluid transition, Comput. Geotechn 75 (2016) 69–79.
[33] Y. Jiang, F. Dufour, G. Chambon, N. Prime, An elastoviscoplastic Herschel–Bulkley model implemented in finite element method with Lagrangian integration point, Submitted to J. Non-Newtonian Fluid Mech.
[34] P.R. de Souza Mendes, R.L. Thompson, A unified approach to model elasto-viscoplastic thixotropic yield-stress materials and apparent yield-stress fluids, Rheol. Acta 52 (7) (2013) 673–694.
[35] F. Ahonguio, L. Jossic, A. Magnin, Influence of surface properties on the flow of a yield stress fluid around spheres, J. Non-Newtonian Fluid Mech. 206 (2014) 57–70.
[36] D.L. Tokpavi, P. Jay, A. Magnin, L. Jossic, Experimental study of the very slow flow of a yield stress fluid past a cylinder, J. Non-Newtonian Fluid Mech. 164 (2009) 35–44.
[37] L. Jossic, F. Ahonguio, A. Magnin, Flow of a yield stress fluid perpendicular to a disc, J. Non-Newtonian Fluid Mech. 191 (2013) 14–24.
[38] D. Fraggedakis, I. Dimakopoulos, J. Tsamopoulos, Yielding the yield-stress analysis: a study focused on the effects of elasticity on the settling of a single spherical particle in simple yield-stress fluids, Soft Matt. (2016), doi:10.1039/C6SM00480F.